molecules

MDPI

Article

Bioinspired Fern-like Fe_2O_3 Functionalized with Pd/PdO Nanoparticles for High-Performance Acetone Sensing

Gaohan Liu [1] and Haihang Wang [2,*]

[1] College of Materials Science and Engineering, Qingdao University, Qingdao 266071, China; xiaonuanhan@163.com
[2] College of Materials Science and Engineering, Liaocheng University, Liaocheng 252000, China
* Correspondence: whh_qd@163.com

Abstract: The accurate monitoring and detection of acetone vapor are essential for environmental and human safety. Consequently, fern-like Fe_2O_3 with hierarchical vein-like structures is synthesized via a concise hydrothermal method. Compared with pure fern-like Fe_2O_3, fern-like Pd/PdO-Fe_2O_3 shows the best acetone-sensing characteristics, in terms of lower operating temperature (180 °C), better selectivity and excellent long-term stability. More importantly, the response value of the Pd/PdO-Fe_2O_3 sensor to 100 ppm acetone reaches as high as 73, which is 55% higher than that of pristine fern-like Fe_2O_3. This enhanced sensing performance can be ascribed to the synergistic effect between Pd/PdO and fern-like Fe_2O_3. On the one hand, Pd/PdO nanoparticles show favorable catalytic activity toward ionized oxygen molecules; meanwhile, the formation of the heterojunction between PdO and fern-like Fe_2O_3 plays an important role. On the other hand, the hierarchical nature of fern-like Fe_2O_3 promotes efficient gas diffusion throughout the structure. Based on its advantages, fern-like Pd/PdO-Fe_2O_3 becomes a satisfactory candidate for acetone gas sensors.

Keywords: fern-like sensor structure; acetone sensing; metal oxide gas sensors; functionalized Pd/PdO-Fe_2O_3 gas sensors

check for updates

Citation: Liu, G.; Wang, H. Bioinspired Fern-like Fe_2O_3 Functionalized with Pd/PdO Nanoparticles for High-Performance Acetone Sensing. *Molecules* **2024**, *29*, 5791. https://doi.org/10.3390/molecules29235791

Academic Editor: Simone Morais

Received: 22 November 2024
Revised: 4 December 2024
Accepted: 6 December 2024
Published: 7 December 2024

Copyright: © 2024 by the authors. Licensee MDPI, Basel, Switzerland. This article is an open access article distributed under the terms and conditions of the Creative Commons Attribution (CC BY) license (https://creativecommons.org/licenses/by/4.0/).

1. Introduction

Acetone is a colorless, volatile organic compound that poses significant health and environmental risks. It is widely used in industrial processes and products such as solvent production, paint thinners, and chemical synthesis, leading to its release into the atmosphere [1,2]. Prolonged exposure to acetone can cause various adverse health effects, including headaches, dizziness, respiratory issues, and skin irritation [3–5]. Furthermore, acetone is also a critical biomarker in medical diagnostics, particularly for diabetes management. Elevated levels of acetone in breath can indicate ketosis, a condition associated with uncontrolled diabetes [5,6]. Therefore, the accurate monitoring and detection of acetone are essential not only for environmental safety but also for early diagnosis and the management of health conditions [7–9]. Given the potential hazards associated with acetone, there is a pressing need to develop effective acetone sensors. Traditional detection methods, such as gas chromatography, are often expensive and require sophisticated laboratory setups, making them impractical for real-time monitoring [10–12]. As a result, the development of reliable, cost-effective, and portable acetone sensors has become a key focus in research and industrial applications.

Metal oxides (MOs) have emerged as promising materials for gas-sensing applications, particularly due to their sensitivity, stability, and ease of fabrication [13–16]. Among the various metal oxide sensors (MOSs), iron oxide (Fe_2O_3) has gained attention as a suitable candidate for acetone detection due to its favorable electronic properties, abundance, and low cost [17–19]. However, while Fe_2O_3 demonstrates promising sensing capabilities, its

performance can be limited by factors such as poor selectivity, high operating temperatures, and inadequate response times [20–22]. Therefore, optimizing its morphology and enhancing its catalytic properties are crucial for improving acetone-sensing performance.

One effective strategy for optimizing the sensing performance of metal oxides is through morphological control. By manipulating the nanoscale structure of metal oxides, researchers can significantly enhance gas diffusion and surface interaction with acetone molecules [23–26]. For instance, hierarchical Fe_2O_3 structures with various morphological properties provide enhanced gas diffusion pathways [27,28]. Similarly, porous NiO architectures offer abundant oxygen adsorption sites, promoting stronger interactions with acetone [29].

The incorporation of noble metals such as silver (Ag) [30,31], platinum (Pt) [32–34], and palladium (Pd) [12,35,36] into these semiconductor matrices can significantly enhance their catalytic properties. These noble metals are known for their superior catalytic activity, which can facilitate reactions at lower temperatures [37–41]. For instance, silver has shown excellent performance in various oxidation reactions, while platinum and palladium are particularly effective in promoting electron transfer processes [37,38,42–44]. The formation of heterojunctions between these noble metals and semiconductor materials can create efficient charge separation, further enhancing overall catalytic efficiency and sensor performance [45–47].

In this work, by optimizing the morphological characteristics of Fe_2O_3 and integrating Pd/PdO to exploit their combined catalytic properties and heterojunction structure, we design and fabricate innovative sensing materials that meet the growing demand for effective and reliable acetone detection. This research not only contributes to the advancement of gas-sensing technology but also highlights the importance of interdisciplinary approaches in addressing real-world challenges.

2. Experimental Procedure

2.1. Preparation of Fern-like Fe_2O_3 and Fern-like Pd/PdO-Fe_2O_3

The preparation process is displayed in Figure 1. Specifically, 0.5 g of $K_3Fe(CN)_6$ was dispersed in 70 mL of distilled water to create a suspension, and the pH was adjusted to 8.0 using 0.1 M ammonia solution. This mixture was then transferred to a 100 mL Teflon-lined stainless-steel autoclave, which was sealed and heated at 170 °C for 12 h before cooling naturally. The resulting product was collected via centrifugation, washed multiple times with deionized water and absolute ethanol, and finally dried in a vacuum at 60 °C, yielding red fern-like Fe_2O_3. As for fern-like Pd/PdO-Fe_2O_3, 0.05 g of fern-like Fe_2O_3 microspheres was dispersed in deionized water under ultrasonic treatment, followed by the addition of 1 mL of $Na_2[PdCl_4]$ (2 mmol L^{-1}) with vigorous agitation. Then, 1 mL of deionized water containing 0.4 mg of $NaBH_4$ was added dropwise to the mixture. After being stirred for approximately 2 h, the mixture was washed with deionized water and absolute ethanol, and then centrifuged. The final powder was calcined at 300 °C for 2 h and labeled as fern-like Pd/PdO-Fe_2O_3.

2.2. Characterization

The characterizations of fern-like Fe_2O_3-based samples were performed using several advanced techniques. X-ray diffraction (XRD) was conducted with a Bruker D8 Advance (Billerica, MA, USA) to analyze crystalline structure, while X-ray photoelectron spectroscopy (XPS) using a Thermo Scientific K-Alpha (Waltham, MA, USA) was employed to determine the surface chemical states and elemental composition. Morphology was examined using scanning electron microscopy (SEM) (JEOL JSM-7500F, Akishima, Japan) and complemented with energy-dispersive spectroscopy (EDS) mapping for elemental distribution. Transmission electron microscopy (TEM) (JEOL JEM-2100F) provided insights into internal structures and particle size, with high-resolution transmission electron microscopy (HRTEM) on the same instrument delivering detailed information on lattice spacing and crystallinity. Together, these techniques offered comprehensive insights into

the structural and compositional features of the synthesized material, highlighting its potential applications in gas sensing and catalysis.

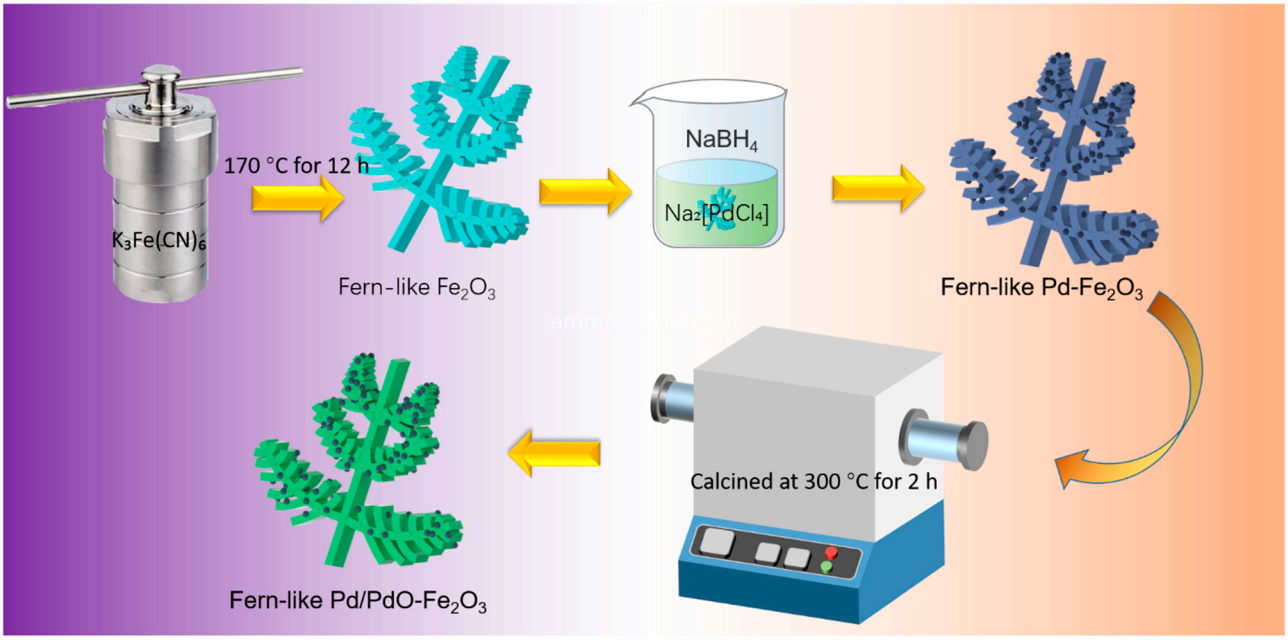


Figure 1. Schematic illustration of the preparation process of Fern-like Pd/PdO-Fe_2O_3.

2.3. Gas Sensor Fabrication and Gas-Sensing Properties Test

The sensor fabrication process involved mixing Fe_2O_3-based sensing materials with ethanol in a 4:1 weight ratio and then grinding the mixture for 20 min to form a paste. This paste was then evenly applied to the surface of a tube with gold electrodes to create the sensing layer. After coating, a Ni-Cr alloy coil was inserted into the ceramic tube to serve as a heater, ensuring precise temperature control. The process concluded with the connecting of the necessary junctions to the sensor sockets. Gas-sensing properties were tested with the WS-60A gas-sensing characterization system (Weisheng Instruments Co. Ltd., Shenzhen, China) using the static liquid–gas distribution method for various gas concentrations, as detailed in the Supplementary Materials. The sensor response (R) is defined as $R = R_a/R_g$, where R_g and R_a represent sensor resistance in the target gas and in dry air, respectively. Response time and recovery time are defined as the time taken to reach 90% of the total resistance change during adsorption and desorption, respectively. To confirm the thickness of the sensing layer, a diagram of its cross-section is illustrated in Figure S1. The thickness of Pd/PdO-Fe_2O_3 is about 20 μm.

3. Results and Discussion

3.1. Structural and Morphological Properties

Figure 2a shows an optical figure of the fern blade in spring. Based on its vein structure, fern-like Fe_2O_3 is designed and synthesized using a concise hydrothermal method. The morphology and microstructure of fern-like Fe_2O_3 are investigated by SEM analysis and the results are illustrated in Figure 2b–d. It can be seen from Figure 2b,c that there are many uniform and independent fern-like Fe_2O_3 structures. A fern-like structure consists of a stem with two groups of highly symmetric, parallel branches. Moreover, the angle between the veins and leaves is about 55°, which is extremely similar to that of the fern blade. This result confirms the successful preparation of fern-like Fe_2O_3. Differently from the green fern blade, the seeds of the fern will grow evenly on the leaves again in the autumn, which allows it to obtain a larger contact area so that the seeds are spread efficiently (Figure 2e). In order to achieve higher gas-sensing efficiency, the Pd/PdO nanoparticles are decorated on the surface of fern-like Fe_2O_3. The surface properties of Pd/PdO-Fe_2O_3 are presented

in Figure 2f–h. After the reduction and calcination processes, the Pd/PdO-Fe_2O_3 retains the initial morphology of fern-like Fe_2O_3. Specifically, as shown in Figure 2h, the Pd/PdO nanoparticles with diameters of 20–50 nm are evenly distributed on the fern-like Fe_2O_3 surface. In addition, Pd/PdO-modified fern-like Fe_2O_3 is characterized using element mapping images. The presence of Fe, O, and Pd can be clearly observed in Figure 2(i1–i4). The distribution of Fe and O is fully consistent with the fern-like hierarchical structure. Meanwhile, the Pd element tends to be evenly dispersed on the fern-like Fe_2O_3 leaf. The microstructure of fern-like Pd/PdO-Fe_2O_3 is explored by TEM and HRTEM, and the images are shown in Figure 2(j1–j4). The light region corresponds to the fern-like Fe_2O_3, while the dark dots represent the Pd/PdO nanoparticles. As shown in Figure 2(j1–j2), all the Pd/PdO nanoparticles are uniformly decorated on the Fe_2O_3 surface, without the existence of serious agglomeration behavior, which can occur upon direct contact with the target gas molecules. To achieve more detailed visualization of Pd/PdO-modified fern-like Fe_2O_3, HRTEM is conducted to explore the interface characteristics of fern-like Pd/PdO-Fe_2O_3, as demonstrated in Figure 2(j3). Obviously, it is easy to observe the interface between the Pd/PdO nanoparticles and fern-like Fe_2O_3, in which the fringe spacing values of 0.224 nm and 0.207 nm can be assigned to the PdO (111) and Fe_2O_3 (202) planes, separately. Figure 2(j4) illustrates the selected area diffraction pattern, and clear diffraction is presented in this figure. These diffraction rings correspond to the (110), (104), and (012) lattice planes of the Fe_2O_3 and the (111) and (102) lattice planes of the Pd/PdO cubic structure. This verifies the polycrystalline nature of the nanoparticles Pd/PdO and fern-like Fe_2O_3.

Figure 3a reveals the XRD pattern of the original fern-like Fe_2O_3 and fern-like Pd/PdO-Fe_2O_3 prepared using the hydrothermal and reduction methods. It can be seen that the diffraction peaks of all samples match well with the rhombohedral structure of α-Fe_2O_3 (JCPDS PDF# 33-0664). The strong characterization peaks located at two-theta angles of 24.1°, 33.2°, 35.6°, 40.9°, 49.5°, 54.1°, 62.5°, 68.3°, 70.1°, and 74.0° can be indexed to the (012), (104), (110), (113), (024), (116), (214), (300), (220), and (018) crystal planes of α-Fe_2O_3, respectively. In addition, the intensity of peaks for α-Fe_2O_3 increases dramatically after high-temperature calcination. This change is often due to variations in crystallinity. Higher temperatures typically promote grain growth, leading to sharper and more intense peaks. However, there is no appearance of typical diffraction peaks for Pd/PdO, which is related to the low-loaded mass of Pd/PdO on the surface of α-Fe_2O_3. No other impurity peak can be observed across the entirety of the XRD pattern, demonstrating that the synthesized Fe_2O_3 sample is a typical composite consisting of Pd/PdO and Fe_2O_3 with excellent purity. The XPS analysis was conducted to explore the surface composition and valence state of all Fe_2O_3 products. As shown in Figure 3b, the full survey spectra of pristine Fe_2O_3 and Pd/PdO-Fe_2O_3 consist of the Fe, O, and Pd elements. Figure 3c shows the high-resolution Fe 2p spectrum, with bending energies at 710 eV and 725 eV corresponding with Fe $2p_{3/2}$ and Fe $2p_{1/2}$, which coincides well with the XRD analysis. Meanwhile, the bonding energy at 718 eV and 732 can be ascribed to the satellite peaks. As depicted in Figure 3d, two kinds of characterization peaks can be found, which attribute corresponding energies of 336.1 and 337.8 eV to the metal Pd and PdO, respectively. In fact, both Pd and PdO reveal excellent catalytic activity toward the acetone, which originates from the calcination treatment of metal Pd nanoparticles. To confirm the effect of decoration with Pd/PdO nanoparticles on Fe_2O_3, different contents of the various oxygen species are investigated comprehensively. The O 1s spectra can be divided into three typical peaks, which consist of lattice oxygen (O_L), vacancy oxygen (O_V), and adsorbed oxygen (O_A), respectively. The percentages of the surface oxygen species are listed in Figure 3e,f. It is obvious that the contents of O_V and O_A increase from 12% to 25% and 3% to 43%, respectively, after surface optimization with Pd/PdO nanoparticles. The increased O_A content is beneficial in enhancing gas-sensing performance by offering additional ionized oxygen species. The large increase in surface-adsorbed oxygen species is due to the existence of the high catalytic activity of Pd/PdO nanoparticles.

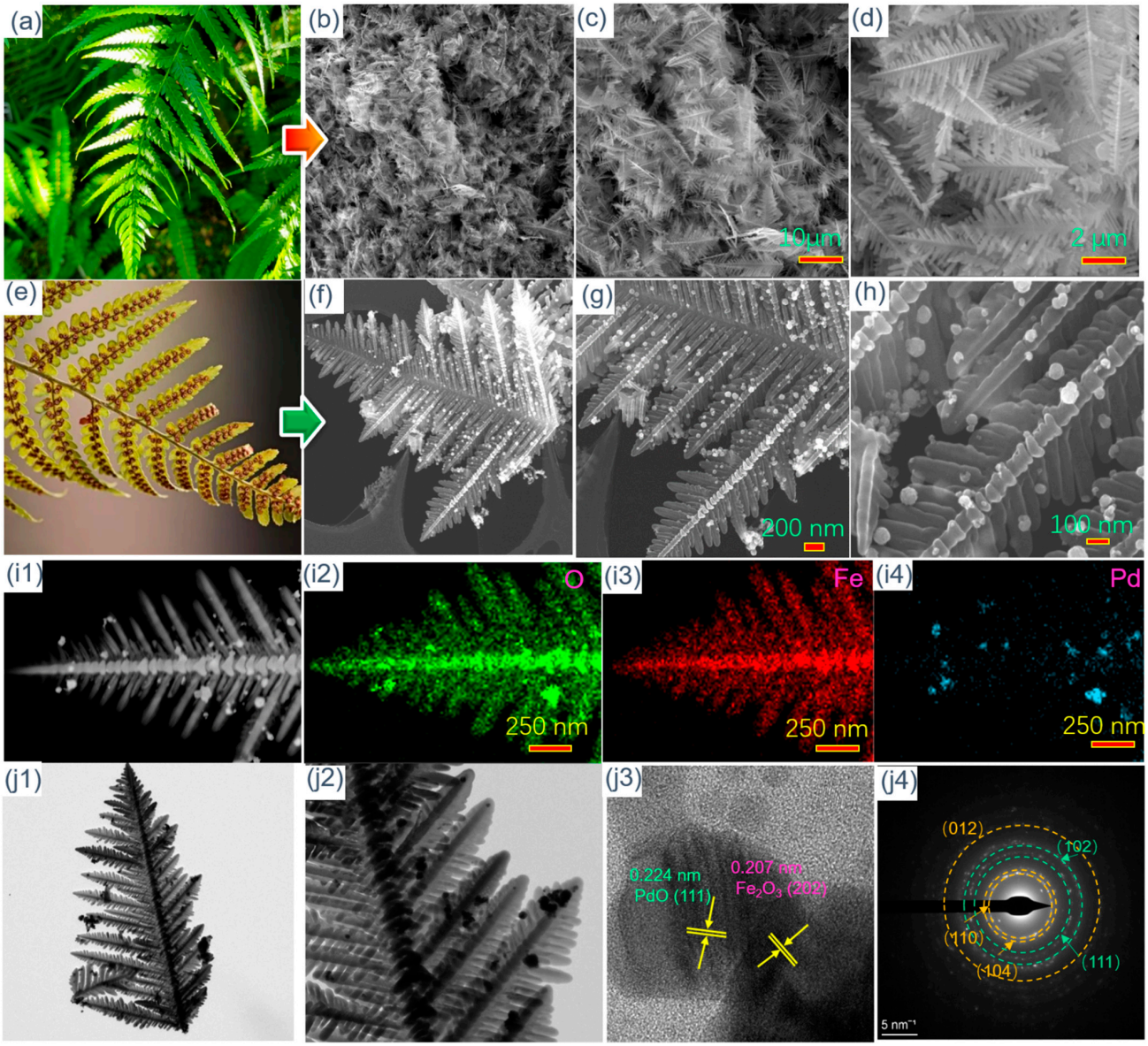


Figure 2. (**a**) An optical figure of the fern blade in (**a**) spring and (**e**) autumn; SEM images of (**b**–**d**) fern-like Fe_2O_3 and (**f**–**h**) fern-like Pd/PdO-Fe_2O_3; (**i1**) HAADF image and the corresponding EDS elemental mapping images of (**i2**) O, (**i3**) Fe, and (**i4**) Pd, respectively; (**j1**–**j2**) TEM, (**j3**) HRTEM images, and (**j4**) area diffraction pattern of fern-like Pd/PdO-Fe_2O_3.

3.2. Sensing Performance

In general, operating temperature has a significant influence on the gas-sensing performance of oxide semiconductors. Therefore, the temperature-dependent responses of Fe_2O_3 sensors toward 100 ppm acetone are recorded to confirm the optimum working temperature. As illustrated in Figure 4a, with increasing temperature, all the Fe_2O_3 sensors show the response tendency of 'volcano' and achieve a maximum response for Fe_2O_3 (47) and Pd/PdO-Fe_2O_3 (73) at 210 °C and 180 °C, respectively. As the sensor works at a low operating temperature, adsorbed gas molecules lack sufficient activity to trigger their gas-sensing reactions, leading to reduced reaction efficiency and lower sensor responses. As optimal operating temperature is reached, the adsorbed gas molecules can obtain enough energy to accelerate the gas-sensing reaction, resulting in a dramatic increase in the response values. Conversely, when the sensing device works in a high-temperature environment (beyond optimal temperature), the gas adsorption state would transform into desorption, leading to decayed sensing performance. Moreover, it can be seen that the

optimum working temperature for Pd/PdO-Fe_2O_3 is lower than that for pure Fe_2O_3. This is due to the enhanced catalytic activity of Pd/PdO, which reduces the activation energy required for gas interactions. Additionally, the modification alters the surface properties of Fe_2O_3, increasing the availability of active sites for gas adsorption. As shown in Figure 4b, the initial resistance values in air of Fe_2O_3 and Pd/PdO-Fe_2O_3 are obtained at different working temperatures in the range from 120 to 270 °C. It is clearly observed that the original resistance values of all sensing devices decrease with increasing operating temperature. In addition, the initial resistance values of Pd/PdO-Fe_2O_3 are higher than those of the pristine Fe_2O_3 sensor. This can be attributed to the electronic properties introduced by Pd/PdO. Pd/PdO can indeed influence resistance by forming heterojunctions at the PdO/Fe_2O_3 interface [29,48]. These heterojunctions introduce energy barriers, which modify the charge carrier dynamics [49]. Additionally, the incorporation of these metallic phases can lead to changes in band structure and charge carrier mobility, resulting in enhanced electron scattering effects. Consequently, the increased resistance in Pd/PdO-Fe_2O_3 reflects the complex interactions between the semiconductor properties of Fe_2O_3 and the metallic characteristics of palladium. The dynamic response–recovery curves of all the sensors to different acetone concentrations (0.1 ppm–100 ppm) at the optimum operating temperature are displayed in Figure 4c. It can be seen that the Pd/PdO-Fe_2O_3 sensor shows the highest response toward acetone under the full concentration range. Figure 4d demonstrates the linear fitting curves of the sensitivity of the two sensors to the acetone concentration. The linear fitting curves for Fe_2O_3 and Pd/PdO-Fe_2O_3 are represented by the equations $y = 0.33x + 11.8$ ($R^2 = 0.98$) and $y = 0.55x + 16.5$ ($R^2 = 0.99$), respectively. Obviously, the response of the Pd/PdO-Fe_2O_3 sensor showed the highest fitting correlation coefficient in accurately detecting the concentration of acetone. When considering the practical application of gas sensors, the response–recovery efficiency is an important parameter to be investigated. Figure 4e,f display the response–recovery dynamic curves of Fe_2O_3 and Pd/PdO-Fe_2O_3 to 80 ppm acetone. The response–recovery times of the pristine Fe_2O_3 and Pd/PdO-Fe_2O_3 are 78/75 s and 11/58s, respectively. Compared to the initial Fe_2O_3 sensor, it can be observed that the incorporation of Pd/PdO nanoparticles dramatically shortens the response–recovery time. This high response–recovery efficiency can be ascribed to the excellent catalytic capability of the Pd/PdO nanoparticles, which can promote the dissociation of the oxygen molecules, therefore enhancing the surface gas-sensing reaction. The adsorbed oxygen species originating from the O1s XPS spectrum also confirms this inference. The selectivity measurements are conducted through the detection of 100 ppm of various gases, including acetone, toluene, xylene, formaldehyde, benzene, ethanol, and methanol, respectively. As revealed in Figure 4g, the Pd/PdO-Fe_2O_3 sensor shows the highest response to all detected gases, verifying the general increase in gas response with the introduction of Pd/PdO nanoparticles. Moreover, it is worth noting that the sensor based on the Pd/PdO-Fe_2O_3 composite has the highest response toward acetone among the various gas molecules, demonstrating good selectivity for acetone gas. In addition to their high gas-sensing properties, the conductometric gas sensors should also possess good reproducibility and long-time stability in actual application. Thereby, the repeatability and long-term stability of Fe_2O_3-based sensors are also explored by applying them to detect 100 ppm acetone at an optimum temperature. As depicted in Figure 4h, after eight successive response–recovery cycles, the Pd/PdO-Fe_2O_3 sensor response is still basically consistent with its first cycle value, indicating the good accuracy and reproducibility of the Pd/PdO-Fe_2O_3 sensor. Subsequently, the long-term stability of Fe_2O_3 and Pd/PdO-Fe_2O_3 sensing devices is investigated by comparing response values (the recording period is five days). The response values over 30 days remain basically unchanged, with the fluctuation being less than 3%, demonstrating that the Pd/PdO-Fe_2O_3 sensor has good long-term stability. In addition, a test of the humidity resistance capability of the Pd/PdO-Fe_2O_3 sensor is conducted as shown in Figure S2. Obviously, it can be seen that the sensor based on Pd/PdO-Fe_2O_3 shows excellent humidity resistance performance.

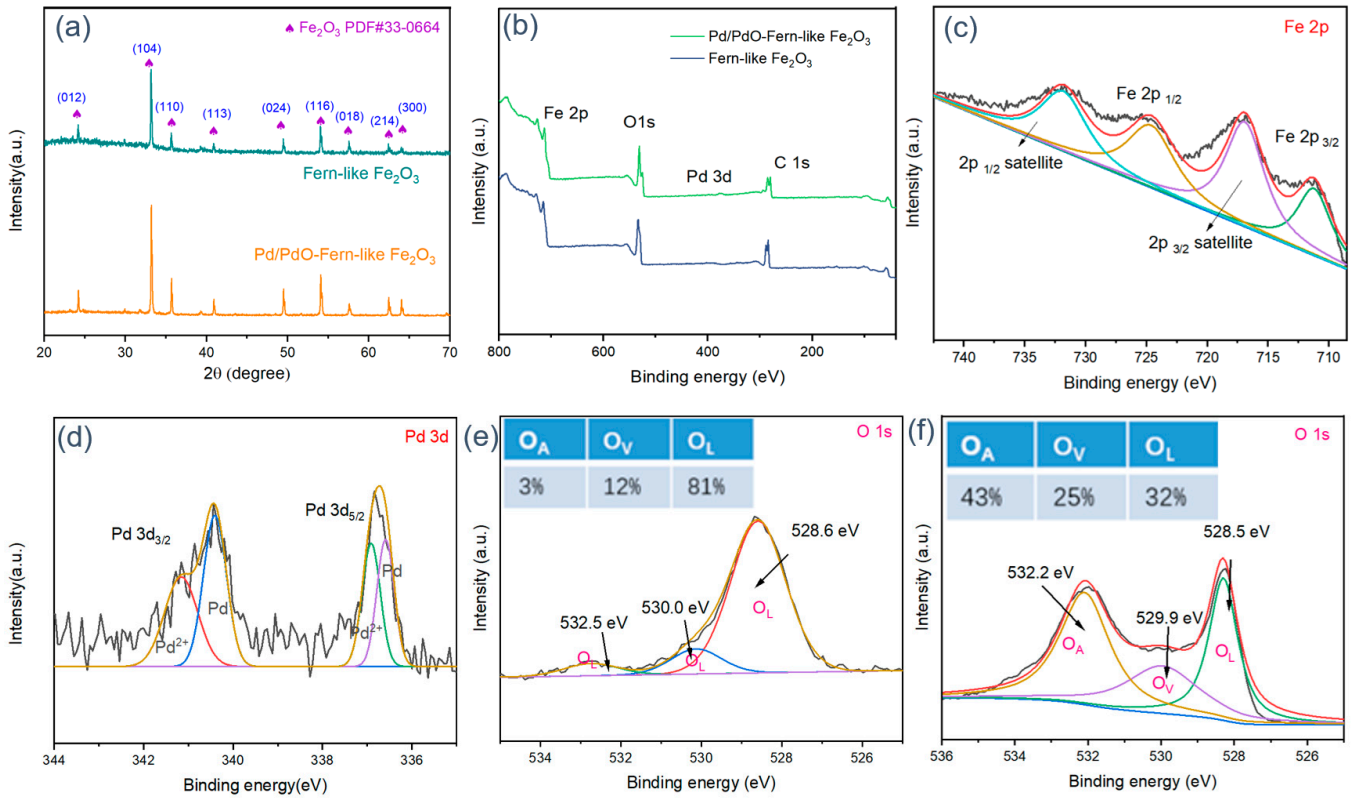


Figure 3. (**a**) XRD pattern and (**b**) XPS spectrum of Fe_2O_3 and Pd/PdO-Fe_2O_3; high-resolution XPS spectrum of (**c**) Fe 2p, (**d**) Pd 3d of Pd/PdO-Fe_2O_3; O 1s spectrum of (**e**) Fe_2O_3 and (**f**) Pd/PdO-Fe_2O_3.

3.3. Sensing Mechanism

It is well known that the gas-sensing performance of a metal oxide semiconductor mainly depends on the resistance change resulting from the adsorption and desorption of gas molecules. Owing to the properties of n-type semiconductors, when the Fe_2O_3-based sensor is exposed to air, the adsorbed oxygen molecules capture electrons from the material conduction band and then ionize into oxygen species containing O_2^-, O^-, and O^{2-} (Equations (1)–(3)). Meanwhile, an electron depletion layer is generated on the surface of the sensing materials, which decreases the electron concentration, increasing the resistance value. Because the working temperature of the Fe_2O_3-based sensor is below 300 °C, O^- is the dominant oxygen species. When the sensor fabricated by Fe_2O_3 is in contact with acetone molecules, the ionized oxygen molecules will interact with acetone molecules and return the free electrons to the sensing materials. This will lead to a decrease in the electron depletion layer and thus a decline in the resistance of the Fe_2O_3 sensor (Equation (4)).

$$O_{2(ads)} + e^- \rightarrow O_2^- (T < 100\ ^\circ C) \quad (1)$$

$$O_{2(ads)} + 2e^- \rightarrow 2O^-_{(ads)}\ (100\ ^\circ C < T < 300\ ^\circ C) \quad (2)$$

$$O_{2(ads)} + 4e^- \rightarrow 2O^{2-}_{(ads)}\ (300\ ^\circ C < T) \quad (3)$$

$$CH_3COCH_3\ (ads) + 8O^-\ (ads) \rightarrow 3CO_2 + 3H_2O + 8e^- \quad (4)$$

Differently from the pure Fe_2O_3 sensor, the sensing performance of the Pd/PdO-Fe_2O_3 sensor has been improved significantly. This result can be attributed to the following reasons. Firstly, the Pd/PdO noble metal on the surface of Fe_2O_3 accelerates the catalytic ionization of oxygen molecules to generate various oxygen species. In fact, noble metals have a high affinity for adsorbing gas molecules and can easily dissociate them into reactive atomic or ionic species. This dissociation lowers the activation energy required for the adsorbed molecules to interact with other surfaces. Once dissociated on the noble metal,

these reactive species are inclined to migrate onto (spillover effect) the adjacent support material. In this case, oxygen atoms adsorbed on Pd/PdO can migrate to Fe_2O_3, promoting more effective electron exchange and enhancing sensor response. The adsorbed oxygen content is confirmed by XPS O1s characterization. Secondly, a Schottky barrier forms between grains due to surface depletion layers. The conductivity of the sensing material relies on electron transport across these grains. Electrons encounter high-energy barriers along their path, which hinder their movement and result in higher surface resistance in the sensor. As shown in Figure 5, a new heterojunction is formed at the interface of PdO and Fe_2O_3. The formation of a Fe_2O_3/PdO heterojunction is primarily driven by the work function difference between Fe_2O_3 and PdO. When these two materials come into contact, electrons will tend to flow from the material with the lower work function (Fe_2O_3) to the material with the higher work function (PdO). This electron transfer continues until an equilibrium is reached, resulting in the formation of a depletion layer at the Fe_2O_3/PdO interface. Finally, the porous and hierarchical nature of fern-like Fe_2O_3 promotes efficient gas diffusion throughout the structure. This allows for rapid interaction between gas molecules and the active sites, enhancing the response and recovery times of the sensor. Therefore, benefiting from the synergistic effect between Pd/PdO and Fe_2O_3, the sensor based on Pd/PdO-Fe_2O_3 shows excellent gas-sensing performance.

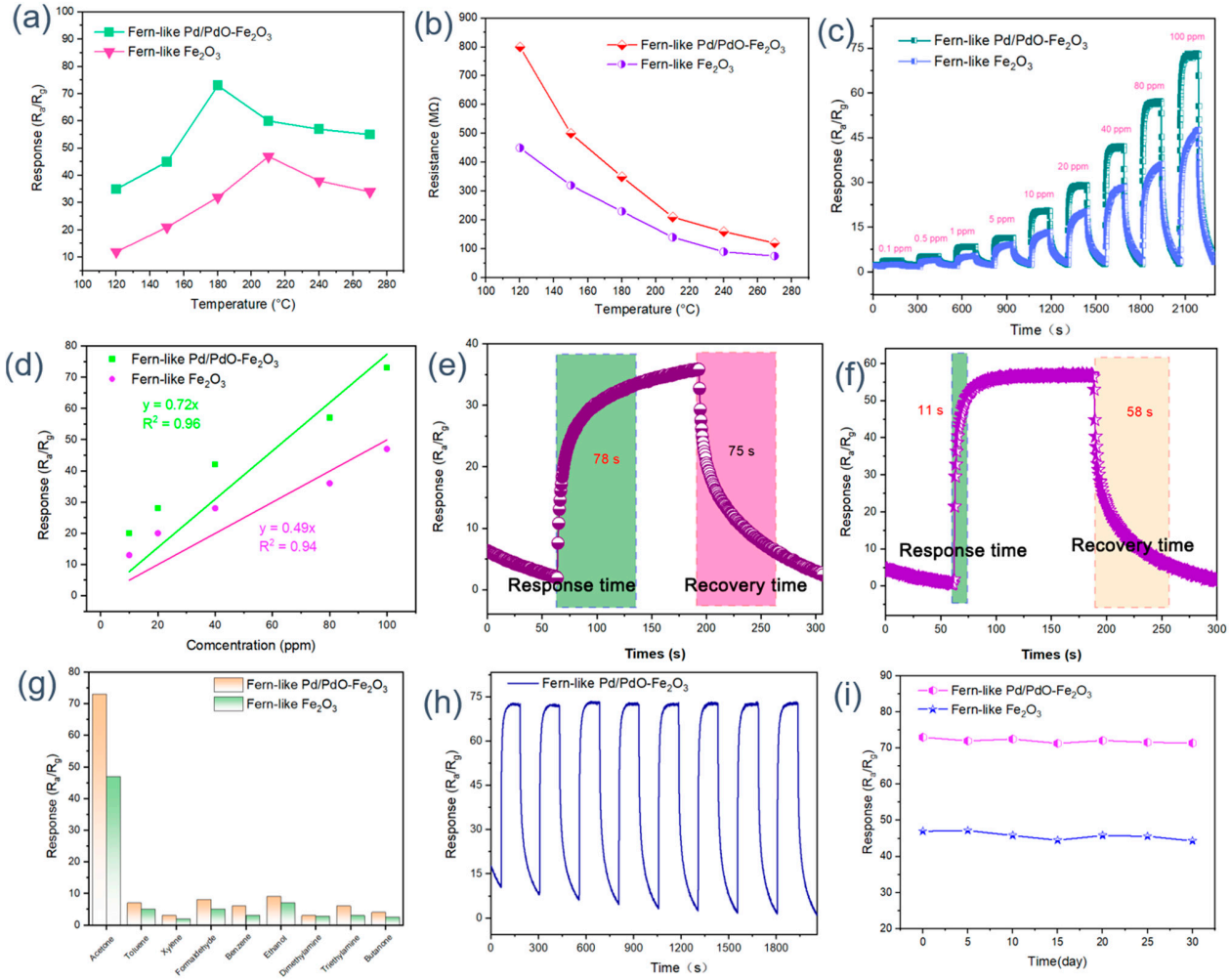


Figure 4. (**a**) Response and (**b**) resistance of all sensors to 100 ppm of acetone at different working temperatures; (**c**) dynamic gas response curves and (**d**) corresponding liner fitting curves of all sensors under different acetone concentrations; response–recovery time of (**e**) pure Fe_2O_3 and (**f**) Pd/PdO-Fe_2O_3 at 80 ppm acetone; (**g**) selectivity, (**h**) reproducibility, and (**i**) long-term stability of Fe_2O_3-based sensors.

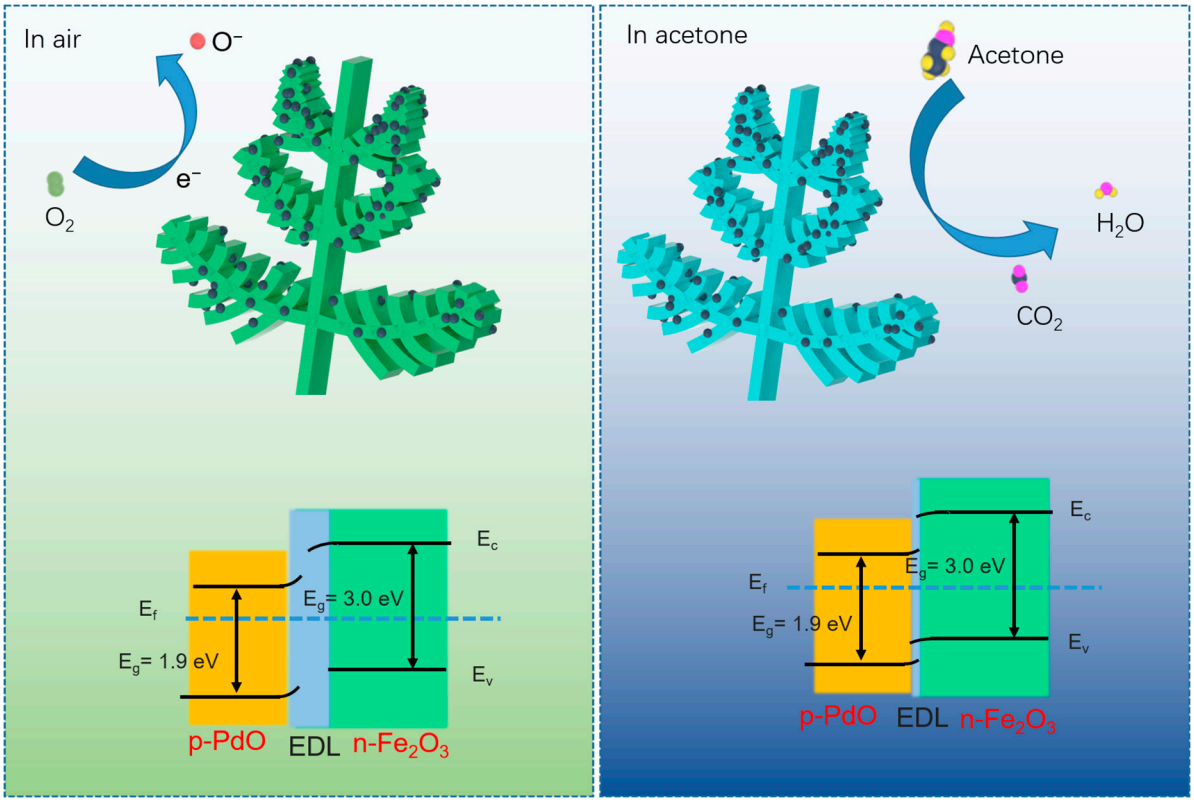


Figure 5. Schematic demonstration of the sensing mechanism of fern-like Pd/PdO-Fe_2O_3-based sensor toward acetone.

4. Conclusions

In summary, fern-like Pd/PdO-Fe_2O_3 with a hierarchical structure is successfully fabricated using a concise hydrothermal–reduction method to achieve enhanced gas-sensing performance. The gas-sensing properties of all Fe_2O_3-based samples are investigated comprehensively. It can be observed that the sensing properties of the fern-like Pd/PdO-Fe_2O_3 sensor are superior to that of the pure fern-like Fe_2O_3 sensor. Specifically, the response value of the fern-like Pd/PdO-Fe_2O_3 sensor to 100 ppm of acetone is about 73, exceeding those of its counterparts (47). In addition, the sensor based on fern-like Pd/PdO-Fe_2O_3 also shows excellent acetone selectivity and favorable long-term stability. This advancement of the fern-like Pd/PdO-Fe_2O_3 sensor in detecting acetone can be attributed to the synergistic effect between highly catalytically active Pd/PdO nanoparticles and fern-like Fe_2O_3. Thus, the sensor based on Pd/PdO-decorated fern-like Fe_2O_3 nanosheets is a promising candidate for high-performance acetone sensors.

Supplementary Materials: The following supporting information can be downloaded at: https://www.mdpi.com/article/10.3390/molecules29235791/s1, Figure S1: Cross-section diagram of Pd/PdO-Fe_2O_3 sensor after sensing test at 180 °C; Figure S2: Humidity resistance capability of Pd/PdO-Fe_2O_3 sensor to 100 ppm of acetone at optimum working temperatures.

Author Contributions: Writing—review & editing, G.L.; Funding acquisition and supervision, H.W. All authors have read and agreed to the published version of the manuscript.

Funding: This research received no external funding

Institutional Review Board Statement: Not applicable.

Informed Consent Statement: Not applicable.

Data Availability Statement: Data are contained within the article and Supplementary Materials.

Acknowledgments: This work was technically supported by the Yuan Ji Cong Analysis and Testing Center. The authors would like to thank the Shiyanjia lab (http://www.shiyanjia.com) for its assistance with the Paper polishing service and the XPS test.

Conflicts of Interest: We declare that we do not have any commercial or associative interests that represents conflicts of interest in connection with the work submitted.

References

1. Maji, B.; Singh, P.; Badhulika, S. A highly sensitive and fully flexible Fe-Co metal-organic framework hydrogel based gas sensor for ppb level detection of acetone. *Appl. Surf. Sci.* **2024**, *678*, 161047. [CrossRef]
2. Lee, J.; Kim, H.; Hilal, M.; Cai, Z. Enhanced acetone gas sensor via TiO_2 nanofiber-NiO nanoparticle heterojunction. *Solid State Sci.* **2024**, *156*, 107683. [CrossRef]
3. Hao, X.; Yu, T.; Meng, X.; Wei, C.; Wang, Y.; Sun, S.; Cheng, P.; Ji, L. Efficient mixed-potential acetone sensor with yttria-stabilized zirconia and porous Co_3O_4 nanofoam sensing electrode for hazardous gas monitoring and breath analysis. *J. Hazard. Mater.* **2024**, *478*, 135462. [CrossRef]
4. Su, Z.; Zhao, Z.; Jin, G.; Chen, W.; Shen, X.; Wu, L. Enhanced acetone gas sensors based on Pt-modified $Co_3O_4/CoMoO_4$ heterojunctions. *Phys. E Low-Dimens. Syst. Nanostruct.* **2024**, *164*, 116042. [CrossRef]
5. Yu, T.; Meng, X.; Hao, X.; Dong, Z.; Wang, Y.; Sun, S.; Cheng, P. YSZ-based mixed-potential acetone sensor with $LaBaCo_2O_5+\delta$ sensitive electrode for diabetic diagnosis. *Sens. Actuators B Chem.* **2024**, *418*, 136273. [CrossRef]
6. Jiang, L.; Lv, S.; Tang, W.; Zhao, L.; Wang, C.; Wang, J.; Wang, T.; Guo, X.; Liu, F.; Wang, C.; et al. YSZ-based acetone sensor using a Cd_2SnO_4 sensing electrode for exhaled breath detection in medical diagnosis. *Sens. Actuators B Chem.* **2021**, *345*, 130321. [CrossRef]
7. Cao, J.; Chen, Y.; Nie, H.; Yan, H. Development of polyimide nanofiber aerogels with a 3D multi-level pore structure: A new sensor for colorimetric detection of breath acetone. *Chem. Eng. J.* **2024**, *496*, 154229. [CrossRef]
8. Chang, X.; Guo, S.; Chen, M.; Zhou, D.; Dong, Z. Synthesis of self-assembled spherical $ZnFe_2O_4$ nanomaterials by the premixed stagnation flame method for highly sensitive acetone sensor. *Sens. Actuators B Chem.* **2024**, *418*, 136216. [CrossRef]
9. Wang, Y.-N.; Qin, L.; Yuan, Z.; Li, J.; Meng, F. UV photosensitized N-CQDs@In_2O_3 ordered porous film elaborated optical fiber acetone gas sensor with ppb-level at room temperature. *Sens. Actuators B Chem.* **2024**, *418*, 136283. [CrossRef]
10. Słupek, E.; Dobrzyniewski, D.; Makoś-Chełstowska, P.; Szulczyński, B.; Gębicki, J. Monitoring of absorptive model biogas purification process using sensor matrices and gas chromatography. *Measurement* **2025**, *239*, 115436. [CrossRef]
11. Verma, A.; Yadav, D.; Natesan, S.; Gupta, M.; Yadav, B.C.; Mishra, Y.K. Advancements in nanohybrid material-based acetone gas sensors relevant to diabetes diagnosis: A comprehensive review. *Microchem. J.* **2024**, *201*, 110713. [CrossRef]
12. Hung, N.P.; Van Duy, N.; Xuan, C.T.; Le, D.T.T.; Hung, C.M.; Jin, H.; Hoa, N.D. Enhanced acetone gas-sensing characteristics of Pd–NiO nanorods/SnO_2 nanowires sensors††Electronic supplementary information (ESI) available. *RSC Adv.* **2024**, *14*, 12438–12448. [CrossRef]
13. Bai, H.; Guo, H.; Tan, Y.; Wang, J.; Dong, Y.; Liu, B.; Xie, Z.; Guo, F.; Chen, D.; Zhang, R.; et al. Facile synthesis of mesoporous CdS/PbS/SnO_2 composites for high-selectivity H_2 gas sensor. *Sens. Actuators B Chem.* **2021**, *340*, 129924. [CrossRef]
14. Bai, H.; Guo, H.; Wang, J.; Dong, Y.; Liu, B.; Xie, Z.; Guo, F.; Chen, D.; Zhang, R.; Zheng, Y. A room-temperature NO_2 gas sensor based on CuO nanoflakes modified with rGO nanosheets. *Sens. Actuators B Chem.* **2021**, *337*, 129783. [CrossRef]
15. Duoc, V.T.; Hung, C.M.; Nguyen, H.; Duy, N.V.; Hieu, N.V.; Hoa, N.D. Room temperature highly toxic NO_2 gas sensors based on rootstock/scion nanowires of SnO_2/ZnO, ZnO/SnO_2, SnO_2/SnO_2 and, ZnO/ZnO. *Sens. Actuators B Chem.* **2021**, *348*, 130652. [CrossRef]
16. Jagannathan, M.; Dhinasekaran, D.; Rajendran, A.R.; Subramaniam, B. Selective room temperature ammonia gas sensor using nanostructured ZnO/CuO@graphene on paper substrate. *Sens. Actuators B Chem.* **2022**, *350*, 130833. [CrossRef]
17. Chen, G.; Tian, R.; Li, Q.; Cao, T.; Tan, H.; Guan, H.; Dong, C.; Comini, E. Enhancing acetone detection of In2O3-decorated MOF-derived Fe_2O_3 spindles with Pt nanoparticles functionalization. *J. Alloys Compd.* **2024**, *1009*, 176998. [CrossRef]
18. Xu, J.; Qu, X.; Yang, W.; Luan, Y.; Ding, X.; Wang, Y.; Guo, L.; Wu, K.; Yang, Z. Oxygen vacancy-mediated metal-organic gel-derived α-Fe_2O_3 for anomalous acetone sensing behavior. *J. Alloys Compd.* **2024**, *995*, 174862. [CrossRef]
19. Wang, Y.; Fan, Y.; Zhu, Y.; Zhu, Z.; Zhou, X.; Zhang, Y.; Mo, S. Ce-doped MIL-101(Fe)-derived CoOx/MnOx@Fe_2O_3 catalysts for photothermal coupled catalytic degradation of acetone and NO. *J. Rare Earths* **2024**, in press. [CrossRef]
20. Mo, R.; Han, D.; Ren, Z.; Yang, D.; Wang, F.; Li, C. Hollow Fe_2O_3/Co_3O_4 microcubes derived from metal-organic framework for enhanced sensing performance towards acetone. *Chin. Chem. Lett.* **2021**, *32*, 3619–3622. [CrossRef]
21. Liu, C.; Xiong, J.; Wang, Y.; Yang, K.; Wang, S.; Zeng, Y. Novel Au-activated SnO_2@Fe_2O_3 hetero-alternated multilayer nanosheets with enhanced low-concentration acetone detection. *Sens. Actuators B Chem.* **2022**, *358*, 131478. [CrossRef]
22. Liu, M.; Ji, J.; Song, P.; Liu, M.; Wang, Q. α-Fe_2O_3 nanocubes/Ti3C2Tx MXene composites for improvement of acetone sensing performance at room temperature. *Sens. Actuators B Chem.* **2021**, *349*, 130782. [CrossRef]
23. Zhang, K.; Li, Y.; Zhang, W. Synthesis of ZnO/α-Fe_2O_3 heterojunction nanocomposites for ultra-sensitive acetone detection. *Mater. Lett.* **2023**, *344*, 134440. [CrossRef]

24. Hu, J.; Xiong, X.; Guan, W.; Chen, Y.; Long, H. Regulation of O-vacancy and heterojunction structure in MOF-derived Fe_2O_3-Co_3O_4 enhancing acetone sensing performance. *Sens. Actuators B Chem.* **2024**, *401*, 135082. [CrossRef]
25. Qin, Q.; Zhang, Y.; Bu, W.; Liu, N.; Zhou, Z.; Hu, C.; Chuai, X. Hierarchical porous Fe_2O_3 derived from willow branch slices biotemplate with fast response and excellent selectivity for acetone. *Sens. Actuators B Chem.* **2023**, *392*, 134079. [CrossRef]
26. Zhao, H.; Li, J.; She, X.; Chen, Y.; Wang, Y.; Zou, C.; Zhou, Y. Black phosphorus nanosheets-sensitized Zn-doped α-Fe_2O_3 nanoclusters for trace acetone detection. *Sens. Actuators B Chem.* **2023**, *395*, 134496. [CrossRef]
27. Mei, H.; Zhou, S.; Lu, M.; Zhao, Y.; Cheng, L. Construction of pine-branch-like α-Fe_2O_3/TiO_2 hierarchical heterostructure for gas sensing. *Ceram. Int.* **2020**, *46*, 18675–18682. [CrossRef]
28. Yang, C.; Yang, Y.; Zhang, C.; Yu, H.; Wang, T.; Shi, K.; Zhang, Z.; Wang, D.; Dong, X. High selectivity of Ag-doped Fe_2O_3 hollow nanofibers in H_2S detection at room operating temperature. *Sens. Actuators B Chem.* **2021**, *341*, 129919. [CrossRef]
29. Li, C.; Choi, P.G.; Kim, K.; Masuda, Y. High performance acetone gas sensor based on ultrathin porous NiO nanosheet. *Sens. Actuators B Chem.* **2022**, *367*, 132143. [CrossRef]
30. Singh, S.; Kumar, G. Ultra-sensitive liquefied petroleum gas (LPG) sensor based on monometallic Ag nanospheres synthesized via microwave-assisted facile approach. *Hybrid Adv.* **2024**, *7*, 100313. [CrossRef]
31. Guo, M.; Wang, B.; Bian, H.; Tao, Z.; Luo, X.; Cui, Y.; Huang, J.; Tu, P. Low-temperature ppm-level H_2S flexible gas sensor on the basis of Ag-modified ZnO. *Mater. Sci. Semicond. Process.* **2025**, *185*, 108944. [CrossRef]
32. Jiang, Y.; Shi, S.; Wang, S.; Du, F.; Wang, P.; Lin, N.; Li, W.; Zhang, Y.; He, L.; Sokolovskij, R.; et al. In-sensor reservoir computing for gas pattern recognition using Pt-AlGaN/GaN HEMTs. *Device* **2024**, 100550, in press. [CrossRef]
33. Lee, J.-H.; Shin, J.-H.; Seo, K.-D.; Park, D.-S.; Shim, Y.-B. 3D printed oxygen gas sensor with a Pt-nanoparticles decorated N-doped carbon catalyst and an amine-polymer composited ionic liquid gel electrolyte. *Sens. Actuators B Chem.* **2025**, *422*, 136657. [CrossRef]
34. Qiao, L.; Jia, X.; Zhang, J.; Yang, J.; Shao, D.; Feng, L.; Song, H. A highly responsive, moisture resistant diabetes diagnostic gas sensor with Pt-loaded porous GO/ZnO. *Sens. Actuators B Chem.* **2024**, *418*, 136275. [CrossRef]
35. Jia, P.; Wang, M.; Ma, C.; Chen, D.; Zhang, Y.; Liu, J. Quantum-level investigation of air decomposed pollutants gas sensor (Pd-modified g-C3N4) influenced by micro-water content. *Chemosphere* **2024**, *358*, 142198. [CrossRef]
36. Li, Z.; Huang, H.; Zhang, Z.; Zhou, J.; Tang, T.; Zhao, D. Room temperature hydrogen gas sensor based on Pd decorated bridging GaN nanowires. *Sens. Actuators B Chem.* **2024**, *417*, 136172. [CrossRef]
37. Tang, M.; Li, Y.; Yang, X. Pt-doped $MoTe_2$ monolayer as a novel sensor for dissolved gases (CH_4, and C_2H_2): A first-principles study. *Chem. Phys. Lett.* **2024**, *857*, 141710. [CrossRef]
38. Zhou, X.; Ying, Z.; Ma, X.; Sheng, W.; Zheng, X. A formaldehyde gas sensor based on Ag-decorated $ZnCo_2O_4$/FF composite. *Chem. Phys. Lett.* **2024**, *842*, 141211. [CrossRef]
39. Yang, M.; Xiong, H.; Ma, Y.; Yang, L. Theoretical investigation of Ag and Au modified CSiN monolayer as a potential gas sensor for air decomposition components detection. *J. Mol. Liq.* **2024**, *410*, 125648. [CrossRef]
40. Verma, A.; Kumar, T. Ag/Cu doped polyaniline hybrid nanocomposite-based novel gas sensor for enhanced ammonia gas sensing performance at room temperature. *RSC Adv.* **2024**, *14*, 25093–25107. [CrossRef] [PubMed]
41. Barbosa, M.S.; Suman, P.H.; Kim, J.J.; Tuller, H.L.; Varela, J.A.; Orlandi, M.O. Gas sensor properties of Ag- and Pd-decorated SnO micro-disks to NO_2, H_2 and CO: Catalyst enhanced sensor response and selectivity. *Sens. Actuators B Chem.* **2017**, *239*, 253–261. [CrossRef]
42. Kang, W.P.; Kim, C.K. Performance and detection mechanism of a new class of catalyst (Pd, Pt, or Ag)-adsorptive oxide (SnOx or ZnO)-insulator-semiconductor gas sensors. *Sens. Actuators B Chem.* **1994**, *22*, 47–55. [CrossRef]
43. Yan, Y.; Luo, Y.; Li, Y.; Zhang, Y.; Wu, P.; Tang, J.; Zhang, X.; Xiao, S. Transition metal (Au, Ni) doped MoS2 as gas sensing materials for C4F7N leakage detection: A comparative study. *Surf. Interfaces* **2024**, *44*, 103625. [CrossRef]
44. Yu, F.; Yuan, H.; Jiang, W.; He, D.; Liu, H.; Qi, X. Comparison of Gas-sensitive response of three metal-doped GaNNT with Pb, Pd and Pt after adsorption of hazardous gases. *Surf. Interfaces* **2024**, *54*, 105170. [CrossRef]
45. Kong, D.L.; Niu, J.Y.; Hong, B.; Xu, J.C.; Han, Y.B.; Peng, X.L.; Ge, H.L.; Li, J.; Zeng, Y.X.; Wang, X.Q. Ag-nanoparticles-anchored mesoporous In_2O_3 nanowires for ultrahigh sensitive formaldehyde gas sensors. *Mater. Sci. Eng. B* **2023**, *291*, 116394. [CrossRef]
46. Mathankumar, G.; Harish, S.; Mohan, M.K.; Bharathi, P.; Kannan, S.K.; Archana, J.; Navaneethan, M. Enhanced selectivity and ultra-fast detection of NO_2 gas sensor via Ag modified WO_3 nanostructures for gas sensing applications. *Sens. Actuators B Chem.* **2023**, *381*, 133374. [CrossRef]
47. Pandey, G.; Bhardwaj, M.; Kumar, S.; Lawaniya, S.D.; Kumar, M.; Dwivedi, P.K.; Awasthi, K. Synergistic effects of Pd-Ag decoration on SnO/SnO_2 nanosheets for enhanced hydrogen sensing. *Sens. Actuators B Chem.* **2024**, *402*, 135062. [CrossRef]
48. Kim, Y.K.; Hwang, S.-H.; Jeong, S.M.; Son, K.Y.; Lim, S.K. Colorimetric hydrogen gas sensor based on PdO/metal oxides hybrid nanoparticles. *Talanta* **2018**, *188*, 356–364. [CrossRef]
49. Luo, Y.; An, B.; Bai, J.; Wang, Y.; Cheng, X.; Wang, Q.; Li, J.; Yang, Y.; Wu, Z.; Xie, E. Ultrahigh-response hydrogen sensor based on PdO/NiO co-doped In_2O_3 nanotubes. *J. Colloid Interface Sci.* **2021**, *599*, 533–542. [CrossRef]

Disclaimer/Publisher's Note: The statements, opinions and data contained in all publications are solely those of the individual author(s) and contributor(s) and not of MDPI and/or the editor(s). MDPI and/or the editor(s) disclaim responsibility for any injury to people or property resulting from any ideas, methods, instructions or products referred to in the content.